HHS Public Access

Author manuscript

NMR Biomed. Author manuscript; available in PMC 2019 February 01.

Published in final edited form as:

NMR Biomed. 2018 February ; 31(2): . doi:10.1002/nbm.3863.

Increased CEST specificity for amide and fast exchanging amine protons using exchange-dependent relaxation rate

Xiao-Yong Zhang[1,2,#], **Feng Wang**[1,2], **Junzhong Xu**[1,2,3,4], **Daniel F. Gochberg**[1,2,3], **John C. Gore**[1,2,3,4,5], and **Zhongliang Zu**[1,2,*]

[1]Vanderbilt University Institute of Imaging Science

[2]Department of Radiology and Radiological Sciences, Vanderbilt University Medical Center

[3]Department of Physics and Astronomy, Vanderbilt University

[4]Department of Biomedical Engineering, Vanderbilt University

[5]Department of Molecular Physiology and Biophysics

Abstract

Chemical exchange saturation transfer (CEST) imaging of amides at 3.5 ppm and fast exchanging amines at 3 ppm provides a unique means to enhance the sensitivity for detecting e.g., proteins/peptides and neurotransmitters, respectively, and hence can provide important information on molecular composition. However, despite the high sensitivity compared to conventional magnetic resonance spectroscopy (MRS), CEST in practice often has relatively poor specificity. For example, CEST signals are typically influenced by several confounding effects including direct water saturation (DS), semi-solid non-specific magnetization transfer (MT), the influence of water relaxation times (T_{1w}) and nearby overlapping CEST signals. Although several editing techniques have been developed to increase the specificity by removing DS, semi-solid MT, and T_{1w} influences, it is still challenging to remove overlapping CEST signals from different exchanging sites. For instance, the amide proton transfer (APT) signal could be contaminated by CEST effects from fast exchanging amines at 3 ppm and intermediate exchanging amines at 2 ppm. The current work applies an exchange-dependent relaxation rate (R_{ex}) to address this problem. Simulations demonstrate that: (1) slowly exchanging amides and fast exchanging amines have distinct dependences on irradiation powers; and (2) R_{ex} serves as a resonance-frequency high-pass filter to selectively reduce CEST signals with resonance frequencies closer to water. These characteristics of R_{ex} provide a means to isolate the APT signal from amines. In addition, previous studies have shown that CEST signals from fast exchanging amines have no distinct features around their resonance frequencies. However, R_{ex} gives Lorentzian lineshapes centered at their resonance frequencies for fast exchanging amines and thus can significantly increase the specificity of CEST imaging for amides and fast exchanging amines.

Graphical abstract

*Correspondence to: Zhongliang Zu, Ph.D., Vanderbilt University Institute of Imaging Science, 1161 21st Ave. S, Medical Center North, AAA-3112, Nashville, TN 37232-2310, zhongliang.zu@vanderbilt.edu, Phone: 615-875-9815, Fax: 615-322-0734.

#This author's current address is: Institute of Science and Technology for Brain-inspired Intelligence, Fudan University, Shanghai, 200433, China

We applied an exchange-dependent relaxation rate R_{ex} to enhance CEST specificity for imaging amide and fast exchanging amine protons. Results show that R_{ex} can correct the shift of CEST peaks in the CEST imaging of fast exchanging amines, and the subtraction of two R_{ex} with a low and a high power (ΔR_{ex}) can successfully remove influences from nearby CEST signals in APT imaging.

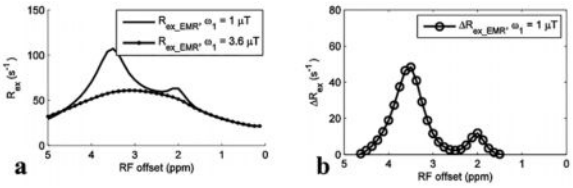

Keywords

MRI; CEST; APT; fast exchanging amine; specificity

INTRODUCTION

Chemical exchange saturation transfer (CEST) is a MRI contrast mechanism for indirectly detecting low-concentration solute molecules with enhanced sensitivity by saturating the solute protons and measuring subsequent changes in the water signal (1). Previously, CEST has been used to detect various endogenous metabolites and macromolecules, such as proteins/peptides (2), creatine (3–6), glutamate (7–12), glucose (13–16), myo-inositol (17), glycogen (18), glycosaminoglycan (19), and lactate (20). Some CEST effects are also sensitive to proton chemical exchange rates and pH (2,21,22). Amide proton transfer (APT) is one widely used form of CEST effect arising from protein backbone amides which resonate at 3.5 ppm from water, and has been used in a range of applications including studies of solid tumors (23–27), ischemic stroke (28–31), and multiple sclerosis (32). Recently, CEST imaging of fast exchanging amines has also been reported. This CEST effect is centered at around 3 ppm from the water resonance which may originate from glutamate amine (7,33) and protein lysine amine (34,35) protons, and which has potential applications in neurological diseases including Alzheimer's disease (8,9), Huntington's disease (10), epilepsy (11), psychosis spectrum (36), and dopamine deficiency (12).

However, although CEST significantly increases the sensitivity for detecting metabolites compared to magnetic resonance spectroscopy (MRS), its specificity in practice is relatively poor: first, CEST can be diminished by non-specific background effects including direct water saturation (DS) and semi-solid magnetization transfer (MT) effects; second, CEST signals may depend on longitudinal relaxation time constant of water (T_{1w}); third, CEST signals from different molecular species overlap. These non-specific factors often vary in pathological tissues, and thus reduce the specificity of CEST for imaging molecular composition. The development of methods to enhance the specificity of CEST imaging is thus important for practical applications.

In order to identify the effect of exchange at a specific frequency, CEST imaging usually acquires a Z-spectrum by employing RF irradiation pulses over a certain range of

frequencies, and the normalized water signals are then analyzed as a function of irradiation frequency (37). Previously, several approaches have been developed to process Z-spectra to isolate the CEST effects from other non-specific signals. For example, an asymmetric analysis (MTR_{asym}) of the Z-spectrum has been used to remove non-specific background signals by assuming that they are symmetric about water. However, in biological tissues, the semi-solid MT is asymmetric, and there are also upfield, relayed nuclear Overhauser enhancement (rNOE) effects (38). Therefore, MTR_{asym} does not accurately report specific information on composition, so to avoid some of these confounding factors, other approaches such as, an extrapolated semi-solid MT reference (EMR) approach (39–41), a Lorentzian difference (LD) analysis (42,43), and a three-point method (21,44) etc. have been developed. To further increase the specificity of CEST metrics, an inverse subtraction method that takes account of variations in T_{1w}, named apparent exchange-dependent relaxation (AREX), was also developed (45–47). Distinct from conventional subtractions of reference and label signals, which can remove only some non-specific background signals, this inverse subtraction can remove a broader range of interactions between CEST and background signals (45).

However, despite these improvements, it is still challenging to remove overlapping CEST signals from nearby exchanging sites. In APT imaging, which is usually performed at relatively low irradiation powers (e.g. 1 μT), nearby intermediate-exchanging amines at 2 ppm may contribute to CEST effects at 3.5 ppm. In addition, our previous study (48) showed that the contributions of fast exchanging amines to CEST signals at 3 ppm are significant even at low irradiation powers, which affect a broad spectral region that overlaps with the APT spectrum centered around 3.5 ppm. Although a multiple-pool Lorentzian fit may potentially separate such overlapping signals (49–53), our study (48) also indicated that fast exchanging amines do not produce Lorentzian lineshapes in CEST spectra, which induces errors to spectral fittings. In CEST imaging of fast exchanging amines, which is usually performed at relatively high irradiation powers (e.g. > 3 μT), the CEST peak shifts, which makes it difficult to identify specific CEST effects (7,54).

In this paper, we apply an exchange-dependent relaxation rate (R_{ex}) for quantifying CEST effects to overcome some of these limitations. R_{ex} was first introduced by Trott and Palmer (55), and later Jin *et al.* (56) showed that R_{ex} can be obtained from CEST Z-spectra in simple model (solute and water) phantoms. More recently, Zaiss *et al.* (45–47) defined a slightly different R_{ex} and showed that this R_{ex} can be obtained from AREX and can be applied in more complex model (solute, semi-solid component, and water) systems and *in vivo*. Note that these two definitions of R_{ex} can be exchangeable with a factor (square of irradiation power/square of irradiation frequency offset). In the rest of this article, we name R_{ex} defined by Zaiss *et al.* as R'_{ex} to avoid any confusion. Since AREX is more suitable to process *in vivo* CEST data, we obtain R_{ex} from the AREX metric by accounting for the irradiation power. The R_{ex} reduces the influences of overlapping CEST signals for APT imaging and provides Lorentzian lineshapes centered at their resonance frequencies (56) for fast exchanging amines, and thus can significantly enhances the CEST detection specificity compared with several previous quantification methods (21,38–40,42–44).

METHODS

The magnetization transfer ratio (MTR) is here defined as the difference between a labelled signal ($S_{lab}(\Delta\omega)$) and a reference signal ($S_{ref}(\Delta\omega)$) normalized by a control signal (S_0) (37),

$$MTR(\Delta\omega)=\frac{S_{ref}(\Delta\omega)-S_{lab}(\Delta\omega)}{S_0} \quad (1)$$

where Δω is the RF frequency offset from the water resonance frequency.

The metric AREX was defined as (47),

$$AREX(\Delta\omega)=(\frac{S_0}{S_{lab}(\Delta\omega)}-\frac{S_0}{S_{ref}(\Delta\omega)})R_{1obs}(1+f_{\mathrm{m}})=\frac{R'_{\mathrm{ex}}(\Delta\omega)}{\cos^2\theta} \quad (2)$$

where

$$\cos^2\theta=\frac{\Delta\omega^2}{\omega_1^2+\Delta\omega^2}$$

R_{1obs} is the apparent water longitudinal relaxation rate, f_m is the semi-solid component concentration, and ω_1 is the irradiation power.

$R'_{ex}(\Delta\omega)$ for fast exchanging pools can be described by (57),

$$R'_{\mathrm{ex}}(\Delta\omega)\approx f_s k_{sw}\underbrace{\frac{\delta\omega_{\mathrm{s}}^2}{\omega_1^2+\Delta\omega^2}}_{a-peak}\frac{\omega_1^2}{\omega_1^2+(R_{2s}+k_{sw})k_{sw}+(\Delta\omega-\delta\omega_{\mathrm{s}})^2k_{sw}/(R_{2s}+k_{sw})} \quad (3)$$

where f_s is the solute concentration, k_{sw} is the exchange rate between solute and water protons, $\delta\omega_s$ is the difference between the water and solute resonance frequencies, and R_{2s} is the solute transverse relaxation rate. The ‘a-peak’ is close to 1 when the irradiation pulse is near the solute resonance frequency, and thus it has weak influence on CEST signals with narrow peaks which could be from slow exchanging pools (e.g. amide) and intermediate exchanging pools (e.g. amine at 2 ppm) at low ω_1. For this reason, the slow and intermediate exchanging pools, that have been described by following Eq. (4), could be also roughly described by Eq. (3).

$$R'_{ex}(\Delta\omega) \approx f_s k_{sw} \frac{\omega_1^2}{\omega_1^2+(R_{2s}+k_{sw})k_{sw}+(\Delta\omega-\delta\omega_s)^2 k_{sw}/(R_{2s}+k_{sw})}. \quad (4)$$

Note that Eq. (4) is a Lorentzian function, whereas Eq. (3) is not.

Here, we normalize AREX by the irradiation power expressed as the square of tan θ, where $\tan^2\theta = \omega_1^2/\Delta\omega^2$.

$$R_{ex}(\Delta\omega)=\frac{AREX(\Delta\omega)}{\tan^2\theta}=f_s k_{sw}\frac{\delta\omega_s^2}{\omega_1^2+(R_{2s}+k_{sw})k_{sw}+(\Delta\omega-\delta\omega_s)^2 k_{sw}/(R_{2s}+k_{sw})} \quad (5)$$

Eq. (5) shows that after normalization by the square of tangent theta, R_{ex} can be obtained from AREX. CEST lineshapes in Eq. (5) are Lorentzian for both slow and fast exchanging regimes. Specifically, for slow exchanging amide pools for which k_{sw} (e.g. 30 s^{-1} (2)) is much less than typical ω_1 (e.g. 1 μT (44,48,52,58,59)), R_{ex} inversely depends on ω_1^2 and is expected to approach 0 at high ω_1; by contrast, for fast exchanging pools for which k_{sw} (e.g. 5000 s^{-1} (7,33–35)) is much greater than ω_1 (e.g. 3.6 μT (7)), R_{ex} is approximately independent of ω_1^2. This is different from AREX which gradually increases at higher ω_1 for slow exchanging pools, and is proportional to ω_1^2 for fast exchanging pools. These characteristics of R_{ex} provide an opportunity to isolate slow exchanging amide protons from fast exchanging amine signals. The subtraction of R_{ex} acquired at a high ω_1 from that at a low ω_1 yields.

$$\Delta R_{ex}(\Delta\omega)=R_{ex}(\Delta\omega)\big|_{low}-R_{ex}(\Delta\omega)\big|_{high} \quad (6)$$

The contributions from fast exchanging pools are relatively independent of irradiation powers, and hence are removed in the subtraction. Therefore, ΔR_{ex} provides a means to detect slow exchanging pools selectively. In addition, both R_{ex} and ΔR_{ex} are proportional to $\delta\omega_s^2$, which serves as a resonance-frequency high-pass filter to reduce the influences of other CEST signals with resonance frequency closer to water. This in turn enhances the detection of APT at the higher frequency offset 3.5 ppm. Because MTR, AREX, R_{ex} and ΔR_{ex} were obtained by several ways including simulations and fitting simulated or measured Z-spectra, different subscripts were used to distinguish the obtaining methods.

Numerical simulations

Two types of numerical simulations were performed. First, in order to study the different dependences on ω_1 and Δω of slow and fast exchanging pools, simulations of two-pool (amide and water or fast exchanging amine and water) models and one-pool (water) model were performed. The two-pool model simulations were used to create labelled signals, and the one-pool model simulations were used to create reference signals for further

quantification. The corresponding metrics are named MTR_{simu}, $AREX_{simu}$, and R_{ex_simu} respectively. Second, to mimic realistic tissues, simulations were performed of a six-pool (amide, intermediate and fast exchanging amines, water, rNOE, and semi-solid component) model and another two-pool (semi-solid component and water) model. The six-pool model simulations were used to create labelled signals, and the two-pool (semi-solid component and water) model simulations were used to create simulated reference signals. Fitted reference signals were also obtained from the following fitting approaches on the six-pool model simulated Z-spectra. Comparisons between the fitted reference signals and the simulated reference signals were performed to evaluate the fitting accuracy. The sequence parameters for the simulations are the same as those used in MR experiments *in vivo* (see below), and the tissue parameters are tabulated in Table 1. R_{1obs} was obtained by using Eq. (7) according to Ref (47),

$$R_{1obs} \approx (R_{1w}+f_m R_{1m})/(1+f_m) \quad (7)$$

where $R_{1w}=1/T_{1w}$ and R_{1m} is the semi-solid component longitudinal relaxation rate.

The coupled Bloch equations can be written as $\frac{d\mathbf{M}}{dt}=\mathbf{AM}+\mathbf{M}_0$, where A is a matrix for the corresponding model. The components of the water and solute magnetizations are each described by three coupled equations. The semi-solid pool has a single coupled equation representing the z component, with a Lorentzian absorption lineshape (49). All numerical calculations of the CEST signals were obtained by integrating the differential equations through the sequence using the ordinary differential equation solver (ODE45) in MATLAB 2013b (Mathworks, Natick, MA, USA).

Animal preparation

All animal experiments were approved by the Institutional Animal Care and Usage Committee of Vanderbilt University. Five healthy rats were included in this study. All rats were immobilized and anesthetized with a 2%/98% isoflurane/oxygen mixture during data acquisition. Respiration was monitored to be stable, and a constant rectal temperature of 37°C was maintained throughout the experiments using a warm-air feedback system (SA Instruments, Stony Brook, NY, USA).

MRI

All measurements were performed using a Varian DirectDrive™ horizontal 9.4T magnet with a 38-mm Litz RF coil (Doty Scientific Inc. Columbia, SC, USA). CEST measurements were performed by applying a continuous wave (CW) irradiation with irradiation duration of 5 s and ω_1 of 1 μT and 3.6 μT before acquisition. Since AREX can only process steady-state CEST signals (45), the 5 s irradiation is performed to ensure that the spin system goes to steady state. Z-spectra with ω_1 of 1 μT were acquired with Δω from −4000 Hz to −2500 Hz with a step size of 500 Hz (−10 ppm to −6.25 ppm with a step size of 1.25 ppm at 9.4 T), −2000 Hz to 2000 Hz with a step size of 50 Hz (−5 ppm to 5 ppm with a step size of 0.125 ppm at 9.4 T), and 2500 Hz to 4000 Hz with a step size of 500 Hz (6.25 ppm to 10 ppm with

a step size of 1.25 ppm at 9.4 T). Z-spectra with ω_1 of 3.6 μT were acquired with Δω from −6500 Hz to −3500 Hz with a step size of 500 Hz (−16.25 ppm to −8.75 ppm with a step size of 1.25 ppm at 9.4 T), −2000 Hz to 2000 Hz with steps of 50 Hz (−5 ppm to 5 ppm with a step size of 0.125 at 9.4 T), and 3500 Hz to 6500 Hz with a step size of 500 Hz (8.75 ppm to 16.25 ppm with a step size of 1.25 at 9.4 T). Control images were acquired with Δω of 100,000 Hz (250 ppm at 9.4 T). The acquisition of a Z-spectrum for each power takes roughly 20 mins. R_{1obs} and f_m were obtained using a selective inversion recovery (SIR) quantitative MT method (60). Specifically, a 1-ms inversion hard pulse was applied to invert the free water pool and the subsequent longitudinal recovery times were set to be 4, 5, 6, 8, 10, 12, 15, 20, 50, 200, 500, 800, 1000, 2000, 4000, and 6000 ms. Spin-echo Echo Planar Imaging (SE-EPI) was used for the readout followed by a saturation pulse train to shorten the total acquisition time as described previously (61). A constant delay time of 3.5 s was set between the saturation pulse train and the next inversion pulse. The SIR quantitative MT takes roughly 6 mins. Before data acquisition, shimming was carefully performed so that the root mean square (RMS) deviation of B_0 was less than 5 Hz. All images were obtained using a single-shot SE-EPI acquisition with triple references for phase correction and matrix size 64 × 64 and field of view 30 mm × 30 mm.

Data analysis

For six-pool model simulations and experiments, to avoid the effects of rNOE and asymmetric MT, we used the EMR method (39–41) to fit reference signals for quantifying CEST signals, and derived the metrics as MTR_{EMR}, $AREX_{EMR}$, R_{ex_EMR}, and ΔR_{ex_EMR}, respectively. Specifically for the EMR, CEST data with Δω from −6500 Hz to −3500 Hz and 3500 Hz to 6500 Hz and ω_1 of 3.6 μT, and with Δω from −4000 Hz to −2500 Hz and 2500 Hz to 4000 Hz and ω_1 of 1.0 μT were fitted to a two-pool MT model (APPENDIX) (54). The reference signals in an offset range from −5 ppm to 5 ppm were then estimated using the fitted parameters and used for calculating the above metrics. Due to the relatively homogenous B_1 field in rat brains, ω_1 used to calculate the tangent theta were from nominal values. We also used the three-point method to quantify APT signals and the asymmetric analysis method to quantify CEST signals from fast exchanging amines, and compared them with EMR. Specifically, the average of two CEST signals at 3 and 4 ppm in Z-spectrum was used as reference signal for the three-point method and the signal on the opposite site of water was used as reference signal for the asymmetric analysis method. Their corresponding R_{ex} metrics were named R_{ex_3pt} and R_{ex_asym}, respectively. To evaluate the accuracy of R_{ex} from these approaches, R_{ex} for amide, fast exchanging amine, and the sum of three pools (amide, intermediate and fast exchanging amine) were also calculated using Eq. (5) and used as standard values. For animal studies, region of interests (ROIs) were chosen from the whole rat brains. All data analyses were performed using MATLAB 2013b (Mathworks, Natick, MA, USA).

RESULTS

Simulated MTR, AREX, and R_{ex} for slow exchanging amides and fast exchanging amines

We got MTR_{simu}, $AREX_{simu}$, and R_{ex_simu} with different ω_1 and Δω using the two-pool (amide and water or fast exchanging amine and water) model simulations, and results are

shown in Fig. 1 and Fig. 2, respectively. For slow exchanging amides, MTR_{simu} (Fig. 1a) increases with ω_1 when it is smaller than 1.5 μT, and decreases at higher ω_1. This non-monotonic dependence may be caused the competitive effects of ω_1 and DS. After correcting for the DS effect by the inverse analysis, $AREX_{simu}$ (Fig. 1c) increases continuously with ω_1. Different from both MTR_{simu} and $AREX_{simu}$, R_{ex_simu} (Fig. 1e) for slow exchanging amides decreases significantly with ω_1 (R_{ex_simu} value at 3.5 μT is roughly 10% of that at 1 μT). For fast exchanging amines, both MTR_{simu} (Fig. 1b) and $AREX_{simu}$ (Fig. 1d) increase with ω_1 in our simulation range. In contrast, R_{ex_simu} (Fig. 1f) of fast exchanging amines is independent of ω_1. This simulation result is in agreement with the predictions of Eq. (5), and demonstrates that the subtraction of the two R_{ex} values acquired with a high and a low ω_1 may remove the influence of fast exchanging amines in APT imaging.

Fig. 2 shows the spectra of these metrics. For slow exchanging amides with ω_1 of 1 μT, the deviation of the R_{ex_simu} peak lineshape (Fig. 2e) caused by the tangent theta normalization is negligible compared with the MTR_{simu} peak lineshape (Fig. 2a) and the $AREX_{simu}$ peak lineshape (Fig. 2c). This result is in agreement with our analysis that the ‘a-peak’ does not influence CEST peaks of slow and intermediate exchanging pools greatly, and thus Eq. (3) can model CEST peaks of slow to fast exchanging pools. For fast exchanging amines, both the central frequency and the lineshape of MTR_{simu} peaks (Fig. 2b) depend on ω_1, suggesting that MTR may misinterpret CEST effects. This agrees with previous reports that MTR_{asym} peaks for fast exchanging pools depend on multiple sequence parameters and cannot be used to identify an effect of exchange at a specific frequency (40,46). Even using AREX to improve specificity (Fig. 2d), the CEST peaks have no distinct features around their resonance frequency offsets. In contrast, R_{ex_simu} peaks (Fig. 2f) have Lorentzian lineshapes centered at 3 ppm without dependence on ω_1.

Fitting references using EMR

Fig 3 shows results of simulating the six-pool model and the measured Z-spectra from rat brains and their corresponding EMR fitted reference spectra with ω_1 of 1 μT and 3.6 μT. The simulated reference spectra using two-pool (semi-solid component and water) model simulations are also provided in Fig. 3a and 3c. The match of the fitted reference spectra (S_{ref}) and the simulated reference spectra indicates the success of the fitting approach. In Fig. 3b and 3d, the match of the Z-spectra and the corresponding fitted reference spectra beyond 5 ppm and −5 ppm also suggests the success of the fitting approach in animals (Sup. Fig. S1 shows that the residuals of the EMR fitting are very small). Table 2 lists the fitted semi-solid MT parameters and simulation parameters in the six-pool model simulations. Note that the fitted parameters are very close to the simulation parameters. Table 3 lists the fitted semi-solid MT parameters in the animal experiments.

Fitted MTR, AREX, R_{ex}, and ΔR_{ex} from simulated Z-spectra with the presence of multiple exchanging pools

For simulations with ω_1 of 1 μT, the APT signal at 3.5 ppm in the MTR_{EMR} spectrum (Fig. 4a) overlaps with nearby CEST signals. These nearby overlapping signals are still present in the $AREX_{EMR}$ spectrum (Fig. 4b). However, the intermediate exchanging amine signal at 2

ppm becomes relatively weak in the R_{ex_EMR} spectrum (Fig. 4d) and the ΔR_{ex_EMR} spectrum (Fig. 4e). This result is also in agreement with the expectation from Eq. (5) that R_{ex} has a resonance-frequency high-pass filter effect. Fig. 4d shows that the R_{ex_EMR} spectrum with ω_1 of 3.6 μT roughly matches the baseline of that with ω_1 of 1 μT. Fig. 4e shows the ΔR_{ex_EMR} spectrum in which both the nearby intermediate exchanging amine at 2 ppm and the fast exchanging amine at 3 ppm are successfully reduced. Fig. 4d also shows that R_{ex_EMR} spectrum is a Lorentzian lineshape centered at its resonance frequency and roughly matches the calculated R_{ex} using Eq. (5) for the sum of three pools (amide, intermediate exchanging amine, and fast exchanging amine). The difference between R_{ex} using Eq. (5) for the sum of three pools and the fast exchanging amine pool is the contributions from the amide and the intermediate exchanging amine which cause ~11% error for quantifying the fast exchanging amine. Fig. 4e also shows that R_{ex_EMR} has ~17% error for quantifying amide compared with R_{ex} using Eq. (5) for amide. Similar conclusion can be also drawn from simulations with other tissue parameters listed in Table 1 (data not shown).

Fig. 5 shows several R_{ex} metrics and/or ΔR_{ex} metric with varied tissue parameters. Note that R_{ex_EMR} is significantly larger than R_{ex} using Eq. (5), but R_{ex_3pt} is significantly smaller than R_{ex} using Eq. (5) for slow exchanging amides. However, ΔR_{ex_EMR} is more close to R_{ex} using Eq. (5) than other two metrics. Also note that both R_{ex_EMR} and R_{ex_asym} are close to R_{ex} using Eq. (5) for fast exchanging amines, although R_{ex_EMR} is larger and R_{ex_asym} is smaller than R_{ex} using Eq. (5).

Experimental MTR, AREX, R_{ex}, and ΔR_{ex}

Fig. 6 shows experimental results from rat brains. Similar to the simulations in Fig. 4, the APT signal at 3.5 ppm acquired with ω_1 of 1 μT overlaps with nearby CEST signals in the MTR_{EMR} spectrum (Fig. 6a), but can be successfully isolated from nearby CEST signals in the ΔR_{ex_EMR} spectrum (Fig. 6e). In addition, the CEST peak acquired with ω_1 of 3.6 μT shows no distinct feature around its resonance frequency offset in the AREX spectrum (Fig. 6c), but shows a clear peak centered at around 3 – 4 ppm in the R_{ex_EMR} spectrum (Fig. 6d). Considering some contributions from APT at 3.5 ppm (around 10% of that acquired with ω_1 of 1 μT based on Fig. 1e) and the range of resonance frequencies of endogenous fast exchanging amines and hydroxyls in biological tissues (0.6 – 3 ppm) (7,13,17), the CEST peaks acquired with ω_1 of 3.6 μT may center at around 3 ppm and thus could originate from glutamate amines (7,33) and/or protein lysine amine protons (34,35) which have resonance frequencies at around 3 ppm. Fig. 7 shows maps of R_{ex_EMR} at 3 ppm with ω_1 of 3.6 μT (predominated by the contrast from fast exchanging amine) and ΔR_{ex_EMR} at 3.5 ppm (predominated by the contrast from amide) from a representative rat brain.

DISCUSSION

In this paper, we show that R_{ex} provides unique features to separate slow exchanging amides from fast exchanging and nearby intermediate exchanging amines and to correct central frequency offset in CEST imaging of fast exchanging pools. Together with EMR fitting to get the reference signal, we applied R_{ex} in imaging animal brains. This in turn significantly

improves the detection specificity of CEST imaging for more accurate quantification of molecules.

The influences of fast exchanging pools have not been comprehensively investigated in APT imaging. However, our results in Fig. 6d show that contributions from fast exchanging amines at 3.5 ppm are roughly 64 % of those from amides at 3.5 ppm with ω_1 of 1 μT, suggesting that they may be a major source of errors in quantifying amide protons. These contaminations would be stronger at relatively higher ω_1, which can be shown from the CEST spectra acquired with ω_1 of 3.6 μT in Fig. 6a and 6d. Contaminations from intermediate exchanging amines at 2 ppm in APT imaging may not be significant at 9.4 T, but would be stronger at lower field strength. Another CEST peak at around 2.7 ppm, which cannot be easily observed in the MTR_{EMR} and $AREX_{EMR}$ spectra with ω_1 of 1 μT in Fig. 6a and 6b, can be clearly shown in the R_{ex_EMR} and ΔR_{ex_EMR} spectra in Fig. 6d and 6e. This peak is buried by the two nearby CEST signals from amides at 3.5 and amines at 2 ppm, and thus is overlooked. However, with the reduction of signals from amines at 2 ppm in the R_{ex_EMR} and ΔR_{ex_EMR} spectra, it can be easily observed. This signal at 2.7 ppm is as narrow as those of amides and intermediate exchanging amines at 2 ppm and thus should be from slow or intermediate exchanging pools. According to previous phantom experiments (7,62), it may originate from phosphocreatine which has a resonance frequency at around 2.7 ppm.

Although previous studies suggest the CEST signal at 3 ppm acquired with high ω_1 using MTR_{asym} originates from glutamate, the reported central frequency of the MTR_{asym} peak is not at 3 ppm, but at 2 ppm (7). Our MTR_{EMR} spectrum with ω_1 of 3.6 μT in Fig. 6a also shows a central frequency at around 2 ppm. It has been reported that the central frequency quantified by MTR depends on multiple sequence and tissue parameters, and thus MTR provides false CEST peaks (54,56). Therefore, based only on CEST measurements, it is challenging to identify the resonance frequencies of the exchanging pools and thus the molecular origin of the CEST signals. The $AREX_{EMR}$ spectrum acquired with ω_1 of 3.6 μT in Fig. 6c does not show any distinct feature, and thus is not appropriate to identify the resonance frequency of exchanging pools. However, the R_{ex_EMR} spectrum in Fig. 6d suggests that this CEST effect with ω_1 of 3.6 μT measures both fast exchanging amines at around 3 ppm and some minor contributions from amides at 3.5 ppm. Hydroxyl-water exchange effects may influence the MTR_{asym} spectra, but not the R_{ex} spectrum because they are closer to the water line (<1 ppm) and thus can be reduced by the resonance-frequency high-pass filter of R_{ex}. This *in vivo* result is also in agreement with previous R_{ex} study on phantoms that R_{ex} can provide distinct feathers for fast exchanging CEST signals (56). The difference between R_{ex} using Eq. (5) for the sum of three pools and the fast exchanging amine pool in Fig. 4d suggests that this method can not remove contaminations from amide and intermediate exchanging amine for quantifying fast exchanging amine. However, this contamination is minor at high power based on our simulations. The measured R_{ex_EMR} on rat brains is $28.3 \pm 3.7\ s^{-1}$ (Fig. 6d), and the simulated R_{ex} with f_s of 0.005 is 60.81 (Fig. 4d). Therefore, we can estimate that the concentration of fast exchanging amines in brain should be roughly an order of magnitude higher than the glutamate concentration. This suggests that protein lysine amines at 3 ppm may be a major contribution (34,35).

In this paper, the EMR method was used to estimate reference signal in a complex tissue model. A previous study (63) indicates that, in order to get reliable fittings of the semi-solid MT parameters, multiple RF powers are necessary. Therefore, we used Z-spectra acquired with two RF powers to fit semi-solid MT parameters in the current work. In other studies (39–41,54,63), several independent semi-solid MT model parameters including T_{1w}/T_{2w} were obtained by fitting CEST data to Eq. (A1). However, our fitting of simulated data indicates that T_{1w}/T_{2w} can not be fitted accurately and this inaccuracy leads to errors to the extrapolated signals near water frequency in our study (Sup. Table. S1 and Sup. Fig. S2). This may be due to the different sampling scheme or ω_1 that used for fitting the semi-solid MT model parameters. Interestingly, we found that two different approaches, i.e. (1) fitting of four independent semi-solid MT model parameters (k_{mw}, T_{2m}, $k_{mw}f_mT_{1w}$, Δ_m) with a roughly estimated T_{1w}/T_{2w} value, or (2) direct fitting of five parameters (k_{mw}, T_{2m}, $k_{mw}f_mT_{1w}$, T_{1w}/T_{2w}, Δ_m) with a limited fitting boundary of T_{1w}/T_{2w}, lead to similar accuracy in the estimation of other CEST parameters and extrapolated MT reference signals. Sup. Table. S2–S3 and Sup. Fig. S3–S4 indicate a successful EMR fitting with four independent parameters and an input of 0.8 times and 1.2 times of T_{1w}/T_{2w} value, respectively. Sup. Table S4 and Sup. Fig. S5 indicate a successful EMR fitting with five independent parameters and a limited fitting boundary ranging from 0 to 1.2 times of T_{1w}/T_{2w} value. In normal rat brains at 9.4 T, T_{1w} and T_{2w} distributions are in a limited range. So we obtained T_{1w}/T_{2w} value of 45 from literature survey (44) and fitted four independent semi-solid MT model parameters in the animal study in this paper. In pathologies with significant variations of T_{1w} and T_{2w}, they can be measured and included in the fittings as constants on a voxel basis. More interestingly, we find that ΔR_{ex} is not significantly influenced by the inaccurate fitting of T_{1w}/T_{2w}, possibly because that the subtraction of two R_{ex} removes the fitting errors. Previous studies (64,65) indicate that the semi-solid pool in biological tissue has super-Lorentzian absorption lineshape. However, their studies also show that MT signals with frequency offsets roughly less than 16 ppm can still be fitted well by Lorentzian lineshape. In addition, another study (49) indicates that the semi-solid MT effect near water resonance can be modeled as Lorentzian lineshape. To avoid the singularity in the super-Lorentzian fitting, we used Lorentzian lineshap for the MT fitting. Here we choose sampling points from −16.25 ppm to −8.75 ppm and 8.75 ppm to 16.25 ppm with ω_1 of 3.6 μT and from −10 ppm to −6.25 ppm and 6.25 ppm to 10 ppm with ω_1 of 1 μT for fitting the semi-solid MT parameters. For the sampling points with ω_1 of 3.6 μT, farther offsets were set to avoid the possible contaminations from fast exchanging amines which are more significant at higher powers. Both experiments in Fig. 6d and simulations in Fig. 4d show that R_{ex} with ω_1 of 3.6 μT is higher than that with ω_1 of 1 μT near 5 ppm. These unmatched curves also cause the negative ΔR_{ex} values near 5 ppm in both Fig. 6e and Fig. 4e. This may be due to that our sampling points for fitting the semi-solid MT are contaminated by fast exchanging amines. Further studies require optimization of these sampling points. In the current study, this fitting error near 5 ppm is far from amide at 3.5 ppm and fast exchanging amine at 3 ppm and thus does not have significant influence on our quantifications. Since 1 μT and 3.6 μT RF irradiation powers have been previously used in detecting CEST signals from amides (44,66) and fast exchanging amines (7), respectively, we evaluated these two powers here. Further studies are necessary to optimize the powers for better sensitivity and specificity.

For quantitative CEST data analyses, it is important to estimate reference signals accurately in order to isolate the true chemical exchange effects from other confounding effects including MT and DS. Unfortunately, there is currently no perfect method for this purpose. In the current work, the EMR approach (39–41) was used for fitting reference signals, but our analysis indicates that the EMR is still not robust. Note that the R_{ex} method introduced here is not limited to the EMR method. Some other methods, such as LD (42,43) and Lorentzian fitting (48), may be combined with R_{ex} as well to evaluate reference signals, although the accuracy of these methods at high powers has not been comprehensively investigated either. Further development of methods for obtaining more accurate reference signals may increase the *in vivo* application of R_{ex}.

Although R_{ex} and ΔR_{ex} can significantly increase specificity, it has several drawbacks. First, ΔR_{ex} has reduced signal to noise ratio (SNR) due to the removal of CEST signals from fast exchanging amines. Further studies may be performed to increase the acquisition efficiency. For instance, the SNR could be increased and the acquisition time could be reduced through optimizing the sampling scheme. In this paper, although dense sampling of Z-spectra was performed to show clear CEST profiles, less sampling points between −5 to 5 ppm and multiple acquisitions at 3.5 ppm could significantly reduce the total acquisition time, increase the SNR for imaging amide, and keep showing a rough CEST profile from fast exchanging amine. Second, R_{ex} and/or ΔR_{ex} requires acquisitions with two ω_1, which lengthen the total acquisition time. Third, the tangent theta is sensitive to B_1 error. For example, there will be 19% error in R_{ex} when B_1 has 10% error. However, B_1 mapping as well as CEST acquisitions with multiple ω_1 have already been used in clinical scanners to increase the specificity of CEST imaging (67). Here, we did not measure B_1 since it is relatively homogenous using animal volume coil. But in situations where B_1 is relatively inhomogeneous, B_1 mapping is also required. Here, our study is focused on 9.4 T and two specific ω_1. The relative contribution from amides and fast exchanging amines on other fields and ω_1 require further studies.

CONCLUSION

Our results show that R_{ex} can correct the shift of CEST peaks from fast exchanging amines and ΔR_{ex} can successfully remove influences from nearby CEST signals in APT imaging. This significantly enhances the detection specificity of CEST imaging to amide and fast exchanging amine protons.

Supplementary Material

Refer to Web version on PubMed Central for supplementary material.

Acknowledgments

Grant Sponsor: R21EB17873, R01CA109106, R01CA184693, R01EB017767

Abbreviations used

CEST chemical exchange saturation transfer

MRS	magnetic resonance spectroscopy
APT	amide proton transfer
MT	magnetization transfer
MTR	magnetization transfer ratio
DS	direct water saturation
LD	Lorentzian difference
T_{1w}	water longitudinal relaxation time
R_{ex}	exchange-dependent relaxation rate
MTR_{asym}	MTR asymmetry analysis
AREX	apparent exchange-dependent relaxation
rNOE	relayed nuclear Overhauser enhancement
k_{sw}	solute-water exchange rate
f_m	semi-solid MT pool concentration
f_s	solute concentration
R_{1obs}	apparent water longitudinal relaxation rate
CW	continuous wave
SNR	signal to noise ratio

References

1. Ward KM, Aletras AH, Balaban RS. A new class of contrast agents for MRI based on proton chemical exchange dependent saturation transfer (CEST). Journal of Magnetic Resonance. 2000; 143(1):79–87. [PubMed: 10698648]
2. Zhou JY, Payen JF, Wilson DA, Traystman RJ, van Zijl PCM. Using the amide proton signals of intracellular proteins and peptides to detect pH effects in MRI. Nature Medicine. 2003; 9(8):1085–1090.
3. Haris M, Singh A, Cai KJ, et al. A technique for in vivo mapping of myocardial creatine kinase metabolism. Nature Medicine. 2014; 20(2):209–214.
4. Haris M, Nanga RPR, Singh A, et al. Exchange rates of creatine kinase metabolites: feasibility of imaging creatine by chemical exchange saturation transfer MRI. Nmr in Biomedicine. 2012; 25(11): 1305–1309. [PubMed: 22431193]
5. Cai KJ, Singh A, Poptani H, et al. CEST signal at 2ppm (CEST@2ppm) from Z-spectral fitting correlates with creatine distribution in brain tumor. Nmr in Biomedicine. 2015; 28(1):1–8. [PubMed: 25295758]
6. Cai KJ, Tain RW, Zhou XJ, et al. Creatine CEST MRI for Differentiating Gliomas with Different Degrees of Aggressiveness. Mol Imaging Biol. 2016; 19(2):225–232.
7. Cai KJ, Haris M, Singh A, et al. Magnetic resonance imaging of glutamate. Nature Medicine. 2012; 18(2):302–306.

8. Haris M, Nath K, Cai KJ, et al. Imaging of glutamate neurotransmitter alterations in Alzheimer's disease. Nmr in Biomedicine. 2013; 26(4):386–391. [PubMed: 23045158]
9. Crescenzi R, DeBrosse C, Nanga RPR, et al. In vivo measurement of glutamate loss is associated with synapse loss in a mouse model of tauopathy. Neuroimage. 2014; 101:185–192. [PubMed: 25003815]
10. Pepin J, Francelle L, Carrillo-de Sauvage MA, et al. In vivo imaging of brain glutamate defects in a knock-in mouse model of Huntington's disease. Neuroimage. 2016; 139:53–64. [PubMed: 27318215]
11. Davis KA, Nanga RPR, Das S, et al. Glutamate imaging (GluCEST) lateralizes epileptic foci in nonlesional temporal lobe epilepsy. Science Translational Medicine. 2015; 7(309)
12. Bagga P, Crescenzi R, Krishnamoorthy G, et al. Mapping the alterations in glutamate with GIuCEST MRI in a mouse model of dopamine deficiency. Journal of Neurochemistry. 2016; 139(3):432–439. [PubMed: 27529288]
13. Chan KWY, McMahon MT, Kato Y, et al. Natural D-glucose as a biodegradable MRI contrast agent for detecting cancer. Magnetic Resonance in Medicine. 2012; 68(6):1764–1773. [PubMed: 23074027]
14. Xu X, Chan KW, Knutsson L, et al. Dynamic glucose enhanced (DGE) MRI for combined imaging of blood-brain barrier break down and increased blood volume in brain cancer. Magnetic Resonance in Medicine. 2015; 74(6):1556–1563. [PubMed: 26404120]
15. Xu X, Yadav NN, Knutsson L, et al. Dynamic Glucose-Enhanced (DGE) MRI: Translation to Human Scanning and First Results in Glioma Patients. Tomography. 2015; 1(2):105–114. [PubMed: 26779568]
16. Wang J, Weygand J, Hwang KP, et al. Magnetic Resonance Imaging of Glucose Uptake and Metabolism in Patients with Head and Neck Cancer. Scientific Reports. 2016; 6:30618. [PubMed: 27461165]
17. Haris M, Cai KJ, Singh A, Hariharan H, Reddy R. In vivo mapping of brain myo-inositol. Neuroimage. 2011; 54(3):2079–2085. [PubMed: 20951217]
18. van Zijl PCM, Jones CK, Ren J, Malloy CR, Sherry AD. MR1 detection of glycogen in vivo by using chemical exchange saturation transfer imaging (glycoCEST). Proceedings of the National Academy of Sciences of the United States of America. 2007; 104(11):4359–4364. [PubMed: 17360529]
19. Ling W, Regatte RR, Navon G, Jerschow A. Assessment of glycosaminoglycan concentration in vivo by chemical exchange-dependent saturation transfer (gagCEST). Proceedings of the National Academy of Sciences of the United States of America. 2008; 105(7):2266–2270. [PubMed: 18268341]
20. DeBrosse C, Nanga RPR, Bagga P, et al. Lactate Chemical Exchange Saturation Transfer (LATEST) Imaging in vivo A Biomarker for LDH Activity. Scientific Reports. 2016:6. [PubMed: 28442741]
21. Jin T, Wang P, Zong XP, Kim SG. MR imaging of the amide-proton transfer effect and the pH-insensitive nuclear overhauser effect at 9. 4 T. Magnetic Resonance in Medicine. 2013; 69(3):760–770. [PubMed: 22577042]
22. Sun PZ, Cheung JS, Wang EF, Lo EH. Association between pH-weighted endogenous amide proton chemical exchange saturation transfer MRI and tissue lactic acidosis during acute ischemic stroke. Journal of Cerebral Blood Flow and Metabolism. 2011; 31(8):1743–1750. [PubMed: 21386856]
23. Salhotra A, Lal B, Laterra J, et al. Amide proton transfer imaging of 9L gliosarcoma and human glioblastoma xenografts. Nmr in Biomedicine. 2008; 21(5):489–497. [PubMed: 17924591]
24. Jones CK, Schlosser MJ, van Zijl PCM, et al. Amide proton transfer imaging of human brain tumors at 3T. Magnetic Resonance in Medicine. 2006; 56(3):585–592. [PubMed: 16892186]
25. Jia GA, Abaza R, Williams JD, et al. Amide Proton Transfer MR Imaging of Prostate Cancer: A Preliminary Study. Journal of Magnetic Resonance Imaging. 2011; 33(3):647–654. [PubMed: 21563248]

26. Zhou JY, Lal B, Wilson DA, Laterra J, van Zijl PCM. Amide proton transfer (APT) contrast for imaging of brain tumors. Magnetic Resonance in Medicine. 2003; 50(6):1120–1126. [PubMed: 14648559]
27. Zhou JY, Tryggestad E, Wen ZB, et al. Differentiation between glioma and radiation necrosis using molecular magnetic resonance imaging of endogenous proteins and peptides. Nature Medicine. 2011; 17(1):130–U308.
28. Sun PZ, Wang EF, Cheung JS. Imaging acute ischemic tissue acidosis with pH-sensitive endogenous amide proton transfer (APT) MRI-Correction of tissue relaxation and concomitant RF irradiation effects toward mapping quantitative cerebral tissue pH. Neuroimage. 2012; 60(1):1–6. [PubMed: 22178815]
29. Sun PZ, Zhou JY, Sun WY, Huang J, van Zijl PCM. Detection of the ischemic penumbra using pH-weighted MRI. Journal of Cerebral Blood Flow and Metabolism. 2007; 27(6):1129–1136. [PubMed: 17133226]
30. Sun PZ, Benner T, Copen WA, Sorensen AG. Early Experience of Translating pH-Weighted MRI to Image Human Subjects at 3 Tesla. Stroke. 2010; 41(10):S147–S151. [PubMed: 20876492]
31. Li H, Zu ZL, Zaiss M, et al. Imaging of amide proton transfer and nuclear Overhauser enhancement in ischemic stroke with corrections for competing effects. Nmr in Biomedicine. 2015; 28(2):200–209. [PubMed: 25483870]
32. Dula AN, Asche EM, Landman BA, et al. Development of Chemical Exchange Saturation Transfer at 7T. Magnetic Resonance in Medicine. 2011; 66(3):831–838. [PubMed: 21432902]
33. Wermter FC, Bock C, Dreher W. Investigating GluCEST and its specificity for pH mapping at low temperatures. Nmr in Biomedicine. 2015; 28(11):1507–1517. [PubMed: 26412088]
34. Zong XP, Wang P, Kim SG, Jin T. Sensitivity and Source of Amine-Proton Exchange and Amide-Proton Transfer Magnetic Resonance Imaging in Cerebral Ischemia. Magnetic Resonance in Medicine. 2014; 71(1):118–132. [PubMed: 23401310]
35. Jin T, Kim SG. High field MR imaging of proteins and peptides based on the amine-water proton exchange effect. ISMRM. 2012:2339.
36. Roalf D, Nanga R, Rupert P, et al. Glutamate Imaging (Glucest) Reveals Lower Brain Glucest Contrast in Patients on the Psychosis Spectrum. Schizophrenia Bulletin. 2017; 43:S49–S49.
37. Zhou JY, van Zijl PCM. Chemical exchange saturation transfer imaging and spectroscopy. Progress in Nuclear Magnetic Resonance Spectroscopy. 2006; 48(2–3):109–136.
38. Zu ZL, Xu JZ, Li H, et al. Imaging Amide Proton Transfer and Nuclear Overhauser Enhancement Using Chemical Exchange Rotation Transfer (CERT). Magnetic Resonance in Medicine. 2014; 72(2):471–476. [PubMed: 24302497]
39. Heo HY, Zhang Y, Lee DH, Hong XH, Zhou JY. Quantitative Assessment of Amide Proton Transfer (APT) and Nuclear Overhauser Enhancement (NOE) Imaging with Extrapolated Semi-Solid Magnetization Transfer Reference (EMR) Signals: Application to a Rat Glioma Model at 4. 7 Tesla. Magnetic Resonance in Medicine. 2016; 75(1):137–149. [PubMed: 25753614]
40. Heo HY, Zhang Y, Jiang SS, Lee DH, Zhou JY. Quantitative Assessment of Amide Proton Transfer (APT) and Nuclear Overhauser Enhancement (NOE) Imaging with Extrapolated Semisolid Magnetization Transfer Reference (EMR) Signals: II. Comparison of Three EMR Models and Application to Human Brain Glioma at 3 Tesla Magnetic Resonance in Medicine. 2016; 75(4): 1630–1639. [PubMed: 26033553]
41. Heo HY, Zhang Y, Burton TM, et al. Improving the Detection Sensitivity of pH-Weighted Amide Proton Transfer MRI in Acute Stroke Patients Using Extrapolated Semisolid Magnetization Transfer Reference Signals. Magnetic Resonance in Medicine. 2017; doi: 10.1002/mrm.26799
42. Jones CK, Polders D, Hua J, et al. In vivo three-dimensional whole-brain pulsed steady-state chemical exchange saturation transfer at 7 T. Magnetic Resonance in Medicine. 2012; 67(6):1579–1589. [PubMed: 22083645]
43. Jones CK, Huang A, Xu JD, et al. Nuclear Overhauser enhancement (NOE) imaging in the human brain at 7 T. Neuroimage. 2013; 77:114–124. [PubMed: 23567889]
44. Xu JZ, Zaiss M, Zu ZL, et al. On the origins of chemical exchange saturation transfer (CEST) contrast in tumors at 9. 4 T. Nmr in Biomedicine. 2014; 27(4):406–416. [PubMed: 24474497]

45. Zaiss M, Bachert P. Exchange-dependent relaxation in the rotating frame for slow and intermediate exchange - modeling off-resonant spin-lock and chemical exchange saturation transfer. Nmr in Biomedicine. 2013; 26(5):507–518. [PubMed: 23281186]
46. Zaiss M, Xu J, Goerke S, et al. Inverse Z-spectrum analysis for spillover, MT-, and T1-corrected steady-state pulsed CEST-MRI-application to pH-weighted MRI of acute stroke. Nmr in Biomedicine. 2014; 27(3):240–252. [PubMed: 24395553]
47. Zaiss M, Zu ZL, Xu JZ, et al. A combined analytical solution for chemical exchange saturation transfer and semi-solid magnetization transfer. Nmr in Biomedicine. 2015; 28(2):217–230. [PubMed: 25504828]
48. Zhang XY, Wang F, Li H, et al. Accuracy in the quantification of chemical exchange saturation transfer (CEST) and relayed nuclear Overhauser enhancement (rNOE) saturation transfer effects. Nmr in Biomedicine. 2017; doi: 10.1002/nbm.3716
49. Zaiss M, Schmitt B, Bachert P. Quantitative separation of CEST effect from magnetization transfer and spillover effects by Lorentzian-line-fit analysis of z-spectra. Journal of Magnetic Resonance. 2011; 211(2):149–155. [PubMed: 21641247]
50. Desmond KL, Moosvi F, Stanisz GJ. Mapping of Amide, Amine, and Aliphatic Peaks in the CEST Spectra of Murine Xenografts at 7 T. Magnetic Resonance in Medicine. 2014; 71(5):1841–1853. [PubMed: 23801344]
51. Wang F, Qi HX, Zu ZL, et al. Multiparametric MRI reveals dynamic changes in molecular signatures of injured spinal cord in monkeys. Magn Reson Med. 2014 in press.
52. Zhang XY, Wang F, Afzal A, et al. A new NOE-mediated MT signal at around-1. 6 ppm for detecting ischemic stroke in rat brain. Magnetic Resonance Imaging. 2016; 34(8):1100–1106. [PubMed: 27211260]
53. Zhang XY, Wang F, Jin T, et al. MR imaging of a novel NOE-mediated magnetization transfer with water in rat brain at 9.4 T. Magnetic Resonance in Medicine. 2016; doi: 10.1002/mrm.26396
54. Zhang XY, Wang F, Li H, et al. CEST imaging of fast exchanging amine pools with corrections for competing effects at 9.4 T. Nmr in Biomedicine. 2017; doi: 10.1002/nbm.3715
55. Trott O, AGP. R1(rho) Relaxation outsie of the Fast-Exchange Limit. Journal of Magnetic Resonance. 2002; 154:157–160. [PubMed: 11820837]
56. Jin T, Autio J, Obata T, Kim SG. Spin-Locking Versus Chemical Exchange Saturation Transfer MRI for Investigating Chemical Exchange Process Between Water and Labile Metabolite Protons. Magnetic Resonance in Medicine. 2011; 65(5):1448–1460. [PubMed: 21500270]
57. Zaiss M, Bachert P. Chemical exchange saturation transfer (CEST) and MR Z-spectroscopy in vivo: a review of theoretical approaches and methods. Physics in Medicine and Biology. 2013; 58(22):R221–R269. [PubMed: 24201125]
58. Li H, Zu ZL, Zaiss M, et al. Imaging of amide proton transfer and nuclear Overhauser enhancement in ischemic stroke with corrections for competing effects. Nmr in Biomedicine. 2015; 28(2):200–209. [PubMed: 25483870]
59. Zhang, XY., Li, H., Xu, JZ., et al. A New MT Signal at −1.6 ppm Via NOE-Mediated Saturation Transfer. ISMRM conference; Toronto, CA. 2015; p. p0999
60. Gochberg DF, Gore JC. Quantitative magnetization transfer imaging via selective inversion recovery with short repetition times. Magnetic Resonance in Medicine. 2007; 57(2):437–441. [PubMed: 17260381]
61. Xu JZ, Li K, Zu ZL, et al. Quantitative magnetization transfer imaging of rodent glioma using selective inversion recovery. Nmr in Biomedicine. 2014; 27(3):253–260. [PubMed: 24338993]
62. Zhang XY, Xie JP, Wang F, et al. Assignment of the Molecular Origins of CEST signals at 2 ppm in Rat Brain. Magnetic Resonance in Medicine. 2017; doi: 10.1002/mrm.26802
63. Henkelman RM, Huang XM, Xiang QS, et al. Quantitative Interpretation of Magnetization-Transfer. Magnetic Resonance in Medicine. 1993; 29(6):759–766. [PubMed: 8350718]
64. Morrison C, Stanisz G, Henkelman RM. Modeling Magnetization-Transfer for Biological-Like Systems Using a Semisolid Pool with a Super-Lorentzian Lineshape and Dipolar Reservoir. Journal of Magnetic Resonance Series B. 1995; 108(2):103–113. [PubMed: 7648009]
65. Morrison C, Henkelman RM. A Model for Magnetization-Transfer in Tissues. Magnetic Resonance in Medicine. 1995; 33(4):475–482. [PubMed: 7776877]

66. Li H, Li K, Zhang XY, et al. R-1 correction in amide proton transfer imaging: indication of the influence of transcytolemmal water exchange on CEST measurements. Nmr in Biomedicine. 2015; 28(12):1655–1662. [PubMed: 26466161]

67. Windschuh J, Zaiss M, Meissner JE, et al. Correction of B1-inhomogeneities for relaxation-compensated CEST imaging at 7T. Nmr in Biomedicine. 2015; 28(5):529–537. [PubMed: 25788155]

68. Hua J, Jones CK, Blakeley J, et al. Quantitative description of the asymmetry in magnetization transfer effects around the water resonance in the human brain. Magnetic Resonance in Medicine. 2007; 58(4):786–793. [PubMed: 17899597]

APPENDIX

Eq. (A1) gives the two-pool MT model,

$$\frac{\mathrm{S}}{S_0}=\frac{\frac{1}{T_{1m}}(k_{mw}f_mT_{1w})+R_{rfm}+\frac{1}{T_{1m}}+k_{mw}}{(k_{mw}f_{\mathrm{m}}T_{1w})(R_{rfm}+\frac{1}{T_{1m}})+[1+(\frac{\omega_1}{2\pi\Delta\omega})^2(\frac{T_{1w}}{T_{2w}})](R_{rfm}+\frac{1}{T_{1m}}+k_{mw})} \quad \text{(A1)}$$

where k_{mw} is the exchange rate between semi-solid and water protons; T_{2w} is the transverse relaxation time of water pool; T_{1m} and T_{2m} are the longitudinal and transverse relaxation times of the semi-solid pool, respectively; R_{rfm} is the RF absorption rate, which depends on the absorption lineshape, $g_m(2\pi\Delta\omega)$ through the relationship $R_{rfm}=\omega_1^2\pi g_m(2\pi\Delta\omega)$,

$$g_m(2\pi\Delta\omega)=\frac{1}{\frac{\pi}{T_{2m}}(1+T_{2m}^2(\Delta\omega-\delta\omega_{\mathrm{m}})^2)} \quad \text{(A2)}$$

where $\delta\omega_m$ is the central resonance frequency of semi-solid pool. Four independent semi-solid MT model parameters (k_{mw}, T_{2m}, $k_{mw}f_mT_{1w}$, $\delta\omega_m$) were obtained by fitting CEST data to Eq. (A1), based on the nonlinear least squares fitting approach, using the Levenberg-Marquardt algorithm. In the fitting, T_{1m} was set to 1 s (39,40). T_{1w}/T_{2w} was calculated using the simulation parameters for all simulation studies and set to be 45 for all animal studies. The T_{1w}/T_{2w} value in animals was obtained by literature survey (44). Table A1 lists the starting points and boundaries of the fit of semi-solid MT model parameters.

Table A1

Starting points and boundaries of MT model parameters.

	Start	Lower	Upper
k_{mw} (s^{-1})	25	0	100
T_{2m} (μs)	16	1	100
$k_{mw}f_mT_{1w}$	2	0	10
$\delta\omega_m$ (ppm)	0	−3	3

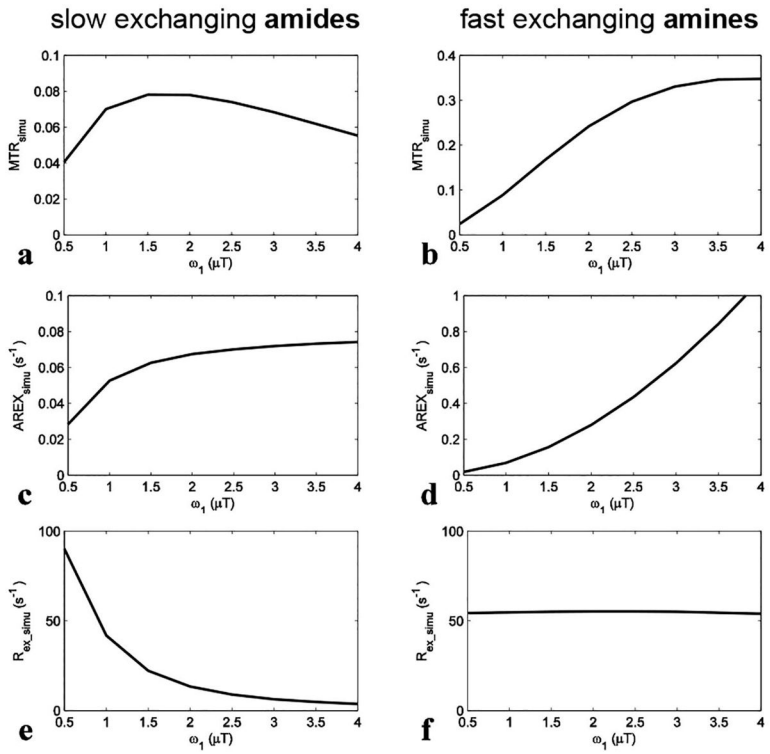

FIG. 1.

Simulated MTR_{simu}, $AREX_{simu}$, and R_{ex_simu} values at 3.5 ppm for slow exchanging amides (a, c, and e) and at 3 ppm for fast exchanging amines (b, d, and f), respectively, vs. ω_1. ω_1 is the irradiation power. The parameters used in simulation were shown in bold in Table 1.

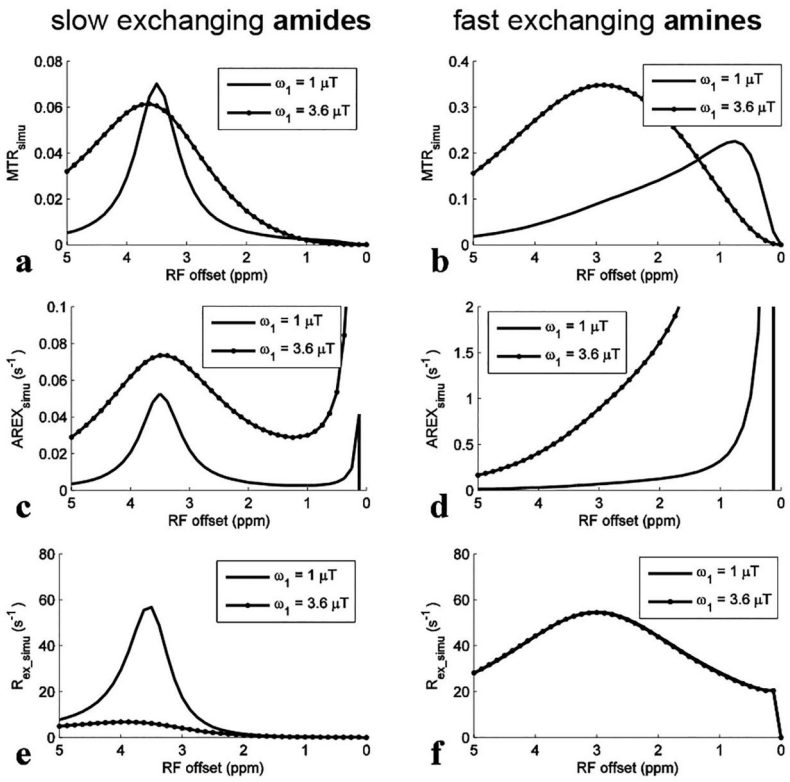

FIG. 2.

Simulated MTR_{simu}, $AREX_{simu}$, and R_{ex_simu} spectra for slow exchanging amides (a, c, and e) and for fast exchanging amines (b, d, and f), respectively, with ω_1 of 1 μT and 3.6 μT. The parameters used in simulation were shown in bold in Table 1.

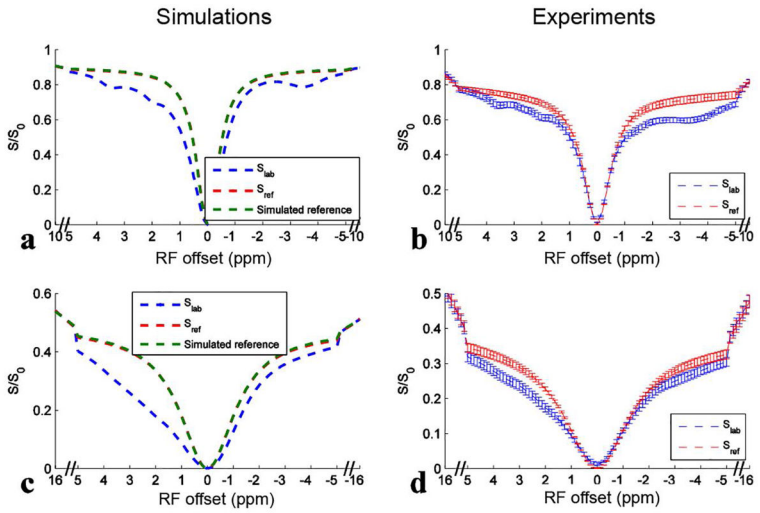

FIG. 3.

Six-pool (amide, intermediate exchanging amine, fast exchanging amine, rNOE, semi-solid MT, and water) model simulated Z-spectra (S_{lab}) and corresponding EMR fitted reference spectra (S_{ref}) (a, c) using values in bold in Table 1, and experimental Z-spectra (S_{lab}) and corresponding EMR fitted reference spectra (S_{ref}) on five healthy rat brains (b, d) with ω_1 of 1 μT (a, b) and 3.6 μT (c, d), respectively. Two-pool (water and semi-solid component) model simulated reference spectra were also shown in (a, c) for comparison with S_{ref} spectra. Note that S_{ref} spectra are covered by the simulated reference spectra, indicating the success of the fitting approach. Error bars in (b, d) represent the standard deviations across subjects.

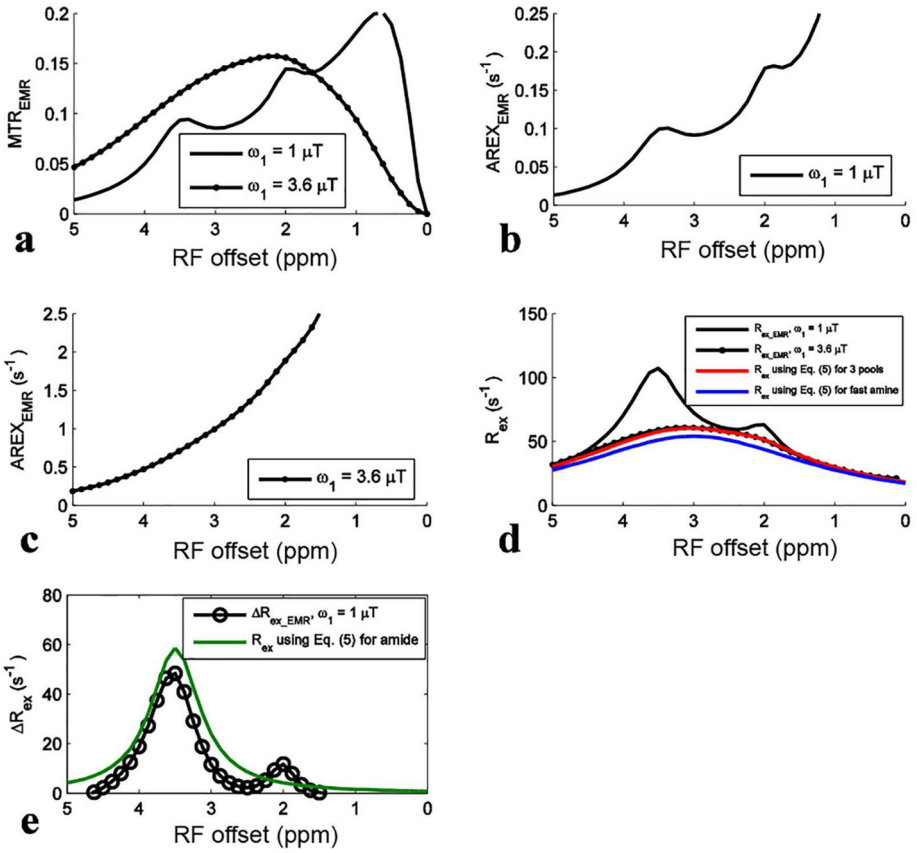

Fig. 4.

Fitted MTR_{EMR} (a), $AREX_{EMR}$ for slow exchanging amides (b), $AREX_{EMR}$ for fast exchanging amines (c), R_{ex_EMR} (d), and ΔR_{ex_EMR} (e) spectra from the six-pool model simulations using values in bold in Table 1. Calculated R_{ex} using Eq. (5) for the sum of three pools (amide, intermediate exchanging amine, and fast exchanging amine) and fast exchanging amine and R_{ex} using Eq. (5) for amide were also shown in (d) and/or (e), for comparison with the fitted metrics.

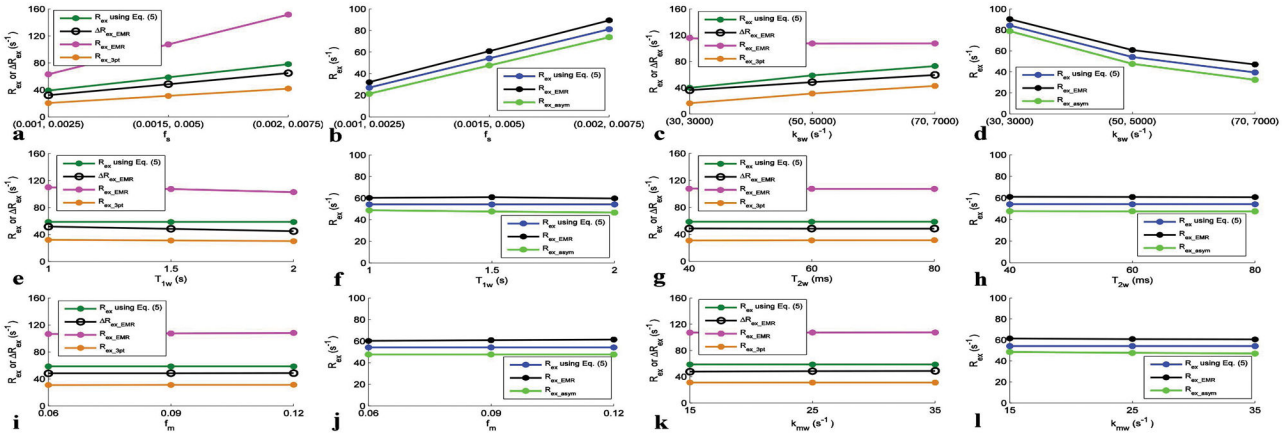

Fig. 5.

R_{ex} and/or ΔR_{ex} with varied amide and fast exchanging amine concentrations (a, b), amide-water and fast exchanging amine-water exchange rates (c, d), T_{1w} (e, f), T_{2w} (g, h), f_m (i, j), and k_{mw} (k, l). Each set of parameters was varied with other parameters remaining at the values in bold in Table 1. 1 μT and 3.6 μT powers are used for getting R_{ex} for slow exchanging amides and fast exchanging amines, respectively.

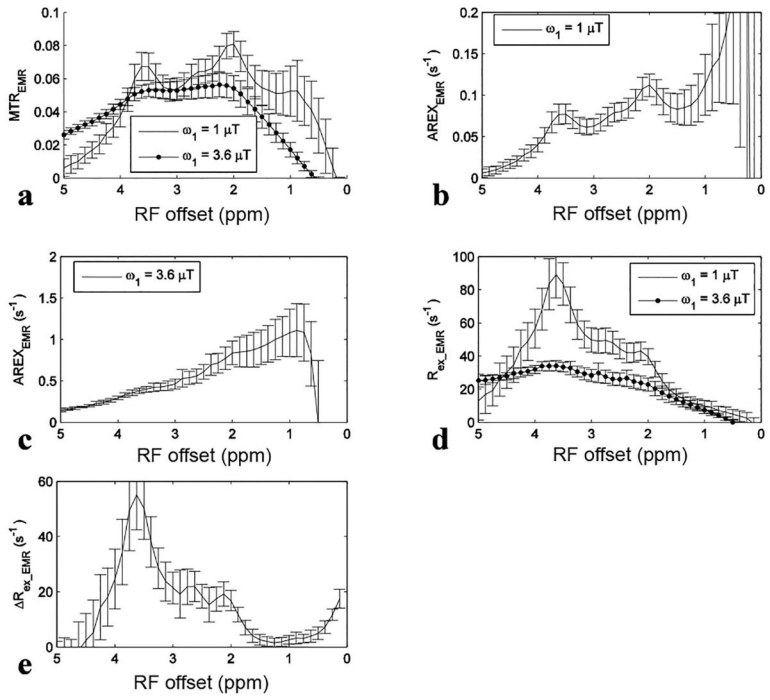

Fig. 6.

Measured MTR_{EMR} (a), $AREX_{EMR}$ for amides (b), $AREX_{EMR}$ for fast exchanging amines (c), R_{ex_EMR} (d), and ΔR_{ex_EMR} (e) spectra on five healthy rat brains. Error bars represent the standard deviations across subjects.

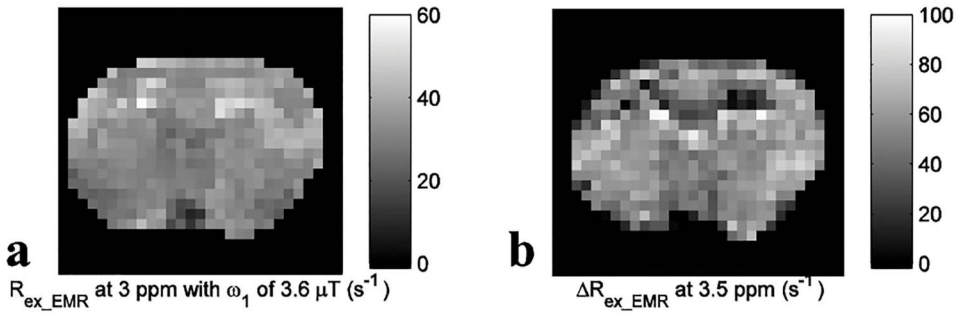

Fig. 7.

Maps of R_{ex_EMR} at 3 ppm with ω_1 of 3.6 μT (a) and ΔR_{ex_EMR} at 3.5 ppm (b) from a representative rat brain

Table 1

Parameters for the multiple model numerical simulations with pool concentration (f), exchange rate (k), longitudinal relaxation time (T_1), transverse relaxation time (T_2), and resonance frequency offset for each pool (δω). Water content is set to be 1.

	water	amide	intermediate exchanging amine	fast exchanging amine	NOE(−3.5)	Semi-solid
f	**1**	0.001,**0.0015**, 0.002	**0.0005**	0.0025, **0.005**, 0.0075	**0.005**	0.06,**0.09**, 0.12
K (s^{-1})	-	30, **50**, 70	**500**	3000, **5000**, 7000	**25**	15, **25**, 35
T_1 (s)	1, **1.5**, 2	**1.5**	**1.5**	**1.5**	**1.5**	**1.5**
T_2 (ms)	40, **60**, 80	**2**	**15**	**15**	**1**	**0.015**
δω (ppm)	**0**	**3.5**	**2**	**3**	**−3.5**	**−2.3**[a]

[a]Ref (68)

Table 2

Fitted semi-solid MT parameters and the simulation parameters in the six-pool model simulations using values in bold in Table 1.

	k_{mw} (s^{-1})	T_{2m} (μs)	$k_{mw}f_mT_{1w}$	$\delta\omega_m$ (ppm)
Fitted	26.9833	16.423	3.5466	−2.0315
simulation	25	15	3.375	−2.3

Table 3

Fitted semi-solid MT parameters for the whole brain in the animal experiments.

n=5	k_{mw} (s^{-1})	T_{2m} (μs)	$k_{mw}f_mT_{1w}$	$\delta\omega_m$ (ppm)
Fitted	17.5 ± 3.1	41 ± 4.1	3.0 ± 0.4	−1.4 ± 0.1